Adjacent backbone interactions control self-sorting of chiral heteroleptic Pd3A2B4 isosceles triangles and Pd4A4C4 pseudo-tetrahedra

Original
Adjacent backbone interactions control self-sorting of chiral heteroleptic Pd3A2B4 isosceles triangles and Pd4A4C4 pseudo-tetrahedra / Benchimol, E., Tessarolo, J., Tarzia, A., Lee, H., Jouaiti, A., Hosseini, M.W., Pavan, G.M., Clever, G.H.. - In: CHEM. - ISSN 2451-9294. - 12:2(2026). [10.1016/j.chempr.2025.102780]

Publisher:
Cell Press - Elsevier

Published
DOI:10.1016/j.chempr.2025.102780

Chem

Article

Adjacent backbone interactions control self-sorting of chiral heteroleptic $Pd_3A_2B_4$ isosceles triangles and $Pd_4A_4C_4$ pseudo-tetrahedra

Graphical abstract

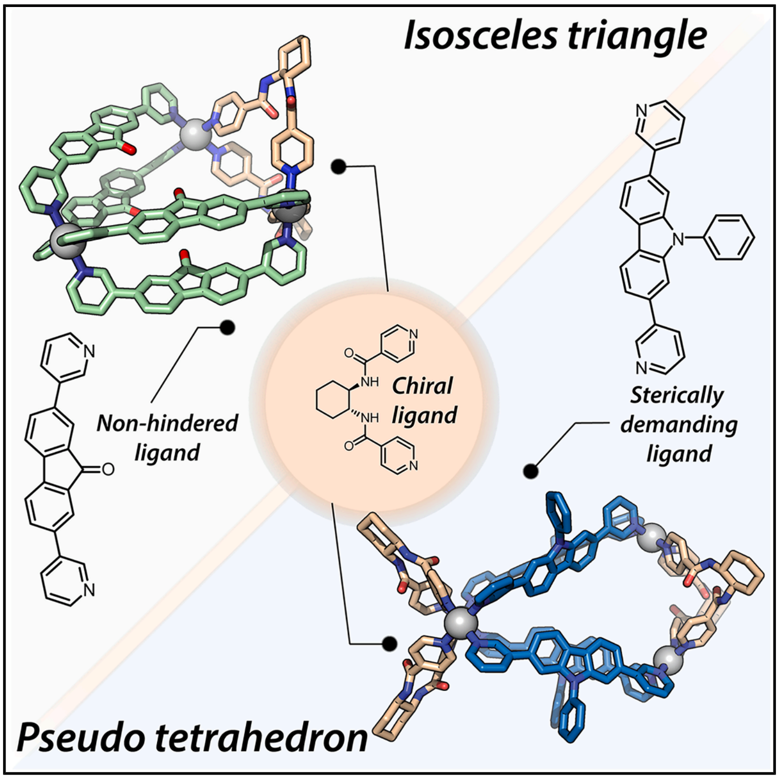

Highlights

- Non-statistical self-assembly of heteroleptic $Pd_3A_2B_4$ isosceles triangles
- Heteromeric narcissistic self-sorting from a mixture of four different ligands
- Structure prediction using a computational toy model
- Selective discrimination of guest enantiomers in self-assembled chiral hosts

Authors

Elie Benchimol, Jacopo Tessarolo, Andrew Tarzia, ..., Mir Wais Hosseini, Giovanni M. Pavan, Guido H. Clever

Correspondence

jacopo@jnu.ac.kr (J.T.),
andrew.tarzia@polito.it (A.T.),
guido.clever@tu-dortmund.de (G.H.C.)

In brief

The precise formation of low-symmetry nanostructures from different building blocks is prevalent in nature but a major challenge in the lab. Recent advances in non-statistical assembly strategies have opened access to intricate structural motifs, combining multiple functionalities. As predicted by a computational toy model, $Pd_3A_2B_4$ isosceles triangles and $Pd_4C_4D_4$ pseudo-tetrahedra form under control of “adjacent backbone interactions” (ABIs). Assembled from four orthogonal ligands, they coexist under heteromeric narcissistic self-sorting conditions and have the ability to discriminate guest enantiomers.

Benchimol et al., 2026, Chem *12*, 102780
February 12, 2026 © 2025 The Author(s).
Published by Elsevier Inc.
https://doi.org/10.1016/j.chempr.2025.102780

Chem

CellPress
OPEN ACCESS

Article

Adjacent backbone interactions control self-sorting of chiral heteroleptic $Pd_3A_2B_4$ isosceles triangles and $Pd_4A_4C_4$ pseudo-tetrahedra

Elie Benchimol,[1] Jacopo Tessarolo,[2,*] Andrew Tarzia,[3,*] Haeri Lee,[4] Abdelaziz Jouaiti,[5] Mir Wais Hosseini,[5]
Giovanni M. Pavan,[3] and Guido H. Clever[1,6,*]
[1]Department of Chemistry and Chemical Biology, TU Dortmund University, Otto-Hahn Str. 6, 44227 Dortmund, Germany
[2]Department of Chemistry, Chonnam National University, Gwangju, Republic of Korea
[3]Department of Applied Science and Technology, Politecnico di Torino, Corso Duca degli Abruzzi 24, 10129 Torino, Italy
[4]Department of Chemistry, Hannam University, Daejeon, Republic of Korea
[5]Laboratoire de Tectonique Moléculaire, UMR 7140 CNRS, Université de Strasbourg, 4 rue Blaise Pascal, Strasbourg, France
[6]Lead contact
*Correspondence: jacopo@jnu.ac.kr (J.T.), andrew.tarzia@polito.it (A.T.), guido.clever@tu-dortmund.de (G.H.C.)
https://doi.org/10.1016/j.chempr.2025.102780

THE BIGGER PICTURE Life's molecular machinery is composed of a multitude of individual proteins and nucleic acids that selectively associate to larger complexes via a combination of weak interactions. Synthetic supramolecular chemistry takes inspiration from this structural and functional complexity, aimed at mimicking and understanding underlying concepts such as heterotopic interactions, non-statistical multicomponent assembly, and dynamic interconversions. Gaining control over the self-sorting of a set of different building blocks to yield a discrete three-dimensional nano-object is not only a challenging goal for advancing synthetic methodology, but it is also crucial to bring multiple functionalities together within a single assembly. Mastering selective multicomponent assembly enables the emergence of sophisticated function, for example, in high-fidelity guest recognition, selective catalysis, or precise placement of photofunctional building blocks in chromophore aggregates. Low-symmetry multicomponent structures of increasing size can now be accessed by metal-mediated self-assembly when exploiting adjacent backbone interactions (ABIs) as a structure-guiding effect. Furthermore, modern computational methods help with predicting plausible assembly outcomes.

SUMMARY

Taking inspiration from biological structures, self-assembled nano-objects promise application potential, e.g., in selective catalysis, smart materials, and drug delivery. While integrating multiple different building blocks greatly enhances their versatility, it is a challenge to design low-symmetry multicomponent structures without generating statistical mixtures. Based on adjacent backbone interactions (ABIs), we introduce here a series of integratively self-sorted Pd_nL_{2n} ($n = 3, 4$) assemblies, each comprising two distinct, easily accessible ligands. In these $Pd_3A_2B_4$ isosceles triangles and $Pd_4A_4C_4$ pseudo-tetrahedra, one ligand is always chiral. Noteworthy, the triangular structures contrast previously described heteroleptic Pd_3L_6 assemblies in that the two differentiable ligands are not contained in equal stoichiometries. The chiral assemblies bind and strongly discriminate chiral guests. They can coexist orthogonally, leading to cage populations under heteromeric narcissistic self-sorting. We further present a computational toy model toward structure prediction of such assemblies, opening avenues for the rational design of discrete metallosupramolecular three-dimensional architectures.

INTRODUCTION

Coordination-driven discrete nanoarchitectures have attracted considerable attention and stand as appealing candidates for mimicking natural host systems such as enzymes. The directionality of bonds between palladium(II) cations and nitrogen heterocycles, together with their dynamic nature, has allowed a myriad of homoleptic assemblies to be rationally constructed or serendipitously discovered. These have been employed in guest separation,[1–6] catalysis under confinement,[7–14] and as bases for advanced materials.[15–17] With the aim to bring their structural and functional complexity even closer to biological receptors and catalysts,[18–21] supramolecular chemistry has recently intensified efforts in development of strategies to create non-statistical heteroleptic assemblies in which multiple components are brought together within a single low-symmetry cage structure.[22–26] Just very recently, populations of such assemblies in which multiple homoleptic or heteroleptic Pd-based structures coexist in a controlled and orthogonal way have started to be described.[27–29] We succeeded to establish a set of synergistic and rational approaches to target formation of such heteroleptic architectures, namely, shape complementary assembly (SCA),[30–33] coordination sphere engineering (CSE),[25,26,34,35] and more recently, adjacent backbone interaction (ABI).[36,37] These proved to be highly instrumental in the design of a series of multifunctional dinuclear species, culminating in the synthesis of maximally self-sorted Pd_2ABCD cages.[38–40]

Design strategies toward non-statistical cage assembly have recently been supported by computational workflows.[22,41–43] However, existing approaches focus on predicting the stability of known structures.[44] Unbiased structure prediction from a set of given building blocks is an expensive task, requiring the evaluation of a large number cage structures (many of which end up as unreasonable, wasted computations).[45] Some of us recently developed an open-source, toy-model approach that can evaluate thousands of structures on ordinary computational hardware in a reasonable time (days), opening the possibility of rapidly predicting hard-to-intuit assemblies.[46]

Most experimental systems reported to date have focused on dinuclear Pd_2L_4 heteroleptic assemblies. However, the employed principles can be translated to higher-order heteroleptic species, and while still scarce, some studies have reported the formation of multicomponent structures with nuclearities of three, four, and even six.[24,36,37,47–49] Specifically, we demonstrated that SCA and ABI can be used to obtain $Pd_3A_3B_3$ and $Pd_4A_4B_4$ rings as well as a heteroleptic $Pd_4A_4C_4$ tetrahedra.[36,37] The functionalization and application of such high-nuclearity heteroleptic architectures are still in their infancy.[36,49] Herein, we report the formation of a family of chiral assemblies for which self-sorting is driven by the degree of steric demand (from small NH or C=O groups to bulky geminal alkyl substituents) installed on the non-chiral ligand component. On the one hand, non-bulky ligands display an unprecedented sorting behavior and assemble with chiral counterparts into isosceles triangular $Pd_3A_2B_4$ rings. On the other hand, the utilization of bulky groups on those ligands generates tetranuclear pseudo-tetrahedral $Pd_4A_4C_4$ architectures. All compounds display intra-assembly ligand-to-ligand chirality transfer, evidenced by chiroptical spectroscopies, as well as the ability to discriminate chiral guests. Eventually, we highlight the formation of cage populations by heteromeric narcissistic self-sorting, composed of either two distinct $Pd_3A_2B_4$ rings or of a $Pd_3A_2B_4$ ring and a $Pd_4A_4C_4$ tetrahedron.

RESULTS AND DISCUSSION

Synthesis of isosceles triangles

All ligands used in this study were synthesized through high-yielding one-step reactions from commercially available reagents, following our established procedures (Figures S1–S3).[23,37] Self-assembly of ligands with Pd(II) cations and formation of the corresponding homoleptic species have been previously reported, except for ligand **L7** (*vide infra*). In particular, enantiopure ligand **L1** (*R,R* enantiomer) leads to the formation of a mixture of homoleptic compounds with a general formula $Pd_n\mathbf{L1}_{2n}$ when combined in a 1:1 ratio with $[Pd(MeCN)_4](BF_4)_2$ in acetonitrile.[50] Ligands **L2**, **L4**, and **L5** all generate mixtures of homoleptic Pd_4L_8 tetrahedra and Pd_3L_6 rings in acetonitrile, while **L3** leads to the tetrahedral assembly exclusively.[23,37,38] We previously showed that the presence of steric bulk in ligands with such bent backbones results in an opposite orientation between the backbone substituent and the pyridine nitrogen in respective assemblies, with a consequent opening of the binding vectors to a ∼90° angle.[37] Due to this effect, **L6** results in the formation of a homoleptic Pd_6L_{12} octahedron when combined with Pd(II). The same principle applies to **L7**, for which we here observed the formation of a similar octahedral Pd_6L_{12} structure with the phenyl groups on the carbazoles directed outside the cavity. **L7** and the octahedron were fully characterized by nuclear magnetic resonance (NMR), electrospray ionization mass spectrometry (ESI-MS), and a single-crystal X-ray structure (Figures S4–S8, S103, and S104). The introduction of steric bulk into this class of ligands has been shown to yield heteroleptic structures through ABI. Indeed, the combination of **L6** with **L2** yielded a discrete $Pd_4A_4B_4$ heteroleptic tetrahedron where the bulkier ligand **L6** occupies the single edges, while ligand **L2** occupies the doubly bridged ones.[37]

Aiming at enhancing both the structural and functional complexity of such higher-nuclearity heteroleptic assemblies, we then extended the system by introducing an enantiomerically pure ligand **L1**. At first, we studied the self-assembly of Pd(II) with **L1** and **L2**, motivated by the fact that **L2** retains its emissive properties in Pd-based assemblies and that **L1** has been shown to successfully transfer its chiral information to another fluorenone-based ligand, resulting in circularly polarized luminescence (CPL).[50] By reacting the components in a 1:1:1 ratio, we obtained a mixture of homoleptic and heteroleptic species. Analyzing the NMR allowed us to identify signals related to the homoleptic species of **L1** as well as another signal set, where particularly four signals from Ha (Figure 2A) of equal intensities caught our attention. Further, DOSY NMR confirmed that all of these signals belonged to the same species with a hydrodynamic radius of 12.7 Å. ESI-MS allowed us to identify the stoichiometry of this compound, resulting in an unprecedented $[Pd_3\mathbf{L1}_2\mathbf{L2}_4{+}n\ BF_4]^{(4-n)+}$ assembly. Thus, when Pd(II) cations and the same ligands **L1** and **L2** were then combined in a 3:2:4 ratio, we were able to exclusively obtain this species (Figures 2B and S9–S16).

While symmetric homoleptic and heteroleptic[36] trinuclear rings have been reported, in-depth analysis of the ^1H NMR splitting, helped by 2D NMR data, reveals the formation of a rather low-symmetrical isosceles triangular ring structure with a previously not reported ligand stoichiometry reminiscent, yet different, of a structure reported earlier by us with a backbone-bridged ligand.[23] The two chiral ligands connect two neighboring Pd(II) ions, while the four fluorenone ligands

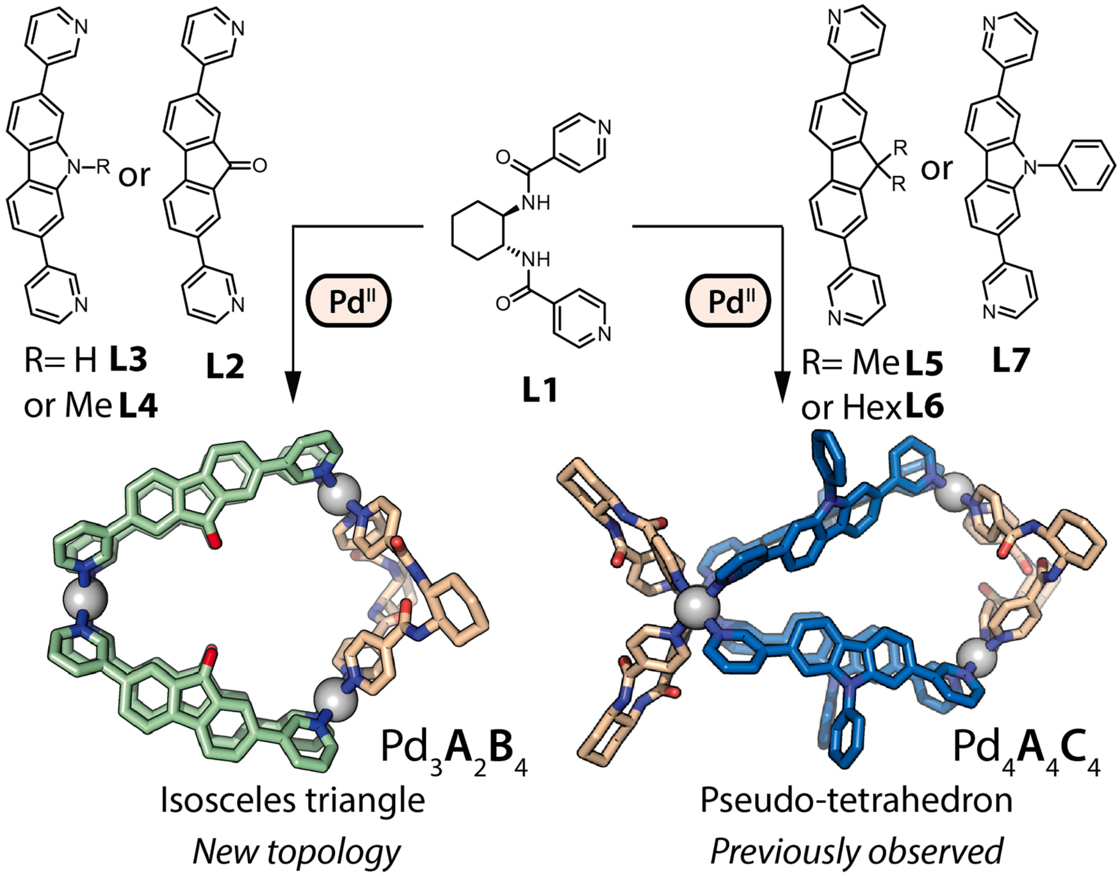

Figure 1. Adjacent backbone interactions drive integrative self-sorting

Adjacent backbone interactions (ABIs) between cyclohexane diamide ligand **L1** and a set of fluorene/carbazole-based ligands **L2**–**L7** allow control over the formation of chiral heteroleptic Pd$_3$**L1**$_2$**Lx**$_4$ (x = 2,3,4) isosceles triangles or Pd$_4$**L1**$_4$**Lx**$_4$ (x = 5,6,7) pseudo-tetrahedra.

L2 complete the ring by bridging those Pd(II) cations with the remaining one. This is evidenced by the ^{1}H-^{1}H ROESY cross-peaks between H1 and H1′ from **L1** and Ha3, Ha4, Hc3, and Hc4 from **L2** (Figure S15). Two Pd(II) centers have therefore a heteroleptic *cis*-environment, while the third is only coordinated by pyridines of **L2**. Owing to the chirality of **L1**, the structure possesses a single C_2 axis passing through the middle of the void between the two ligands **L1** and the opposite Pd(II) center. All four pyridines of the two ligands **L2** on the same side with respect to the ring plane are thus inequivalent (highlighted by different colors in Figure 3C), creating a 4-fold splitting of **L2**, while **L1** protons split into two sets. This topology is further supported by two distinct sets of ^{1}H-^{1}H ROESY cross-peaks between Ha3 and Ha4 on one side and Ha1 and Ha2 on the other (Figure S15). To strengthen the reliability and versatility of this strategy to form unsymmetrical heteroleptic rings, we expanded the scope of non-chiral ligands to a series of other compounds, having a similar bent backbone but different steric bulk (**L3**–**L7**; Figure 1). **L3** and **L4**, having less or similar backbone hindrance, yielded the same Pd$_3$A$_2$B$_4$ structure (Figures S17–S30), while larger substituents (**L5**–**L7**) yielded a different outcome (*vide infra*).

Computational structure prediction using minimal models

Having experimental evidence for the formation of a structure with the unexpected stoichiometry Pd:**L1**:**L2** equal to 3:2:4 and indications of the building block configuration, we turned to computational approaches to better understand the structure of this assembly and to obtain insights into reasons why this is selected among the theoretically possible ones. We implemented a computational structure prediction algorithm that relies only on the input of building block structures and target stoichiometries (complete computational details are available in the supplemental information). Because many possible structures could be derived, we use low-cost toy-model simulations.[46] This new, open-source approach is built on the software *stk*[51] and OpenMM[52] for efficient geometry optimizations (Figures S91–S99; Section S6).

Our toy-model approach simplifies chemical complexity to a few key geometrical features. Here, we have mapped **L1** to a rigid ligand template (Figure 2C; note that this version of the model does not encode stereochemistry into the **L1** model and is inherently an approximation of that geometry) and a twistable ligand template (Figure 2C; Section S6); the distinction is necessary to represent rotations in the pyridine groups. This mapping

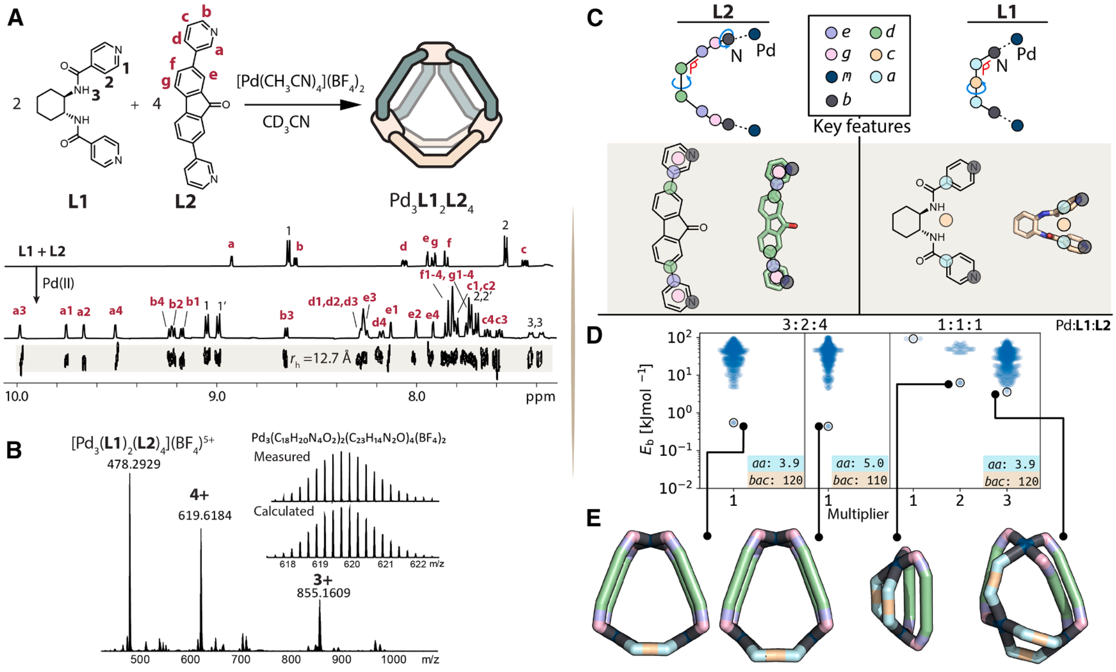

Figure 2. Assembly of the low-symmetry Pd_3L1$_2$L2$_4$ three-membered ring and its toy-model prediction

(A) Self-assembly of **L1** and **L2** with Pd(II) yields a Pd_3**L1**$_2$**L2**$_4$ ring. ^{1}H NMR (trideuteroacetonitrile [CD_3CN], 500 MHz) stack of both ligands mixed and after the addition of Pd(II). Assignment and ^{1}H DOSY NMR traces are given on the spectra.

(B) HR-ESI-MS of an acetonitrile solution of Pd_3**L1**$_2$**L2**$_4$. The inset highlights the measured and calculated isotopic pattern.

(C) Mapping between atomistic and toy models for first-pass structure prediction.

(D) Energy per building block (E_b) of all generated structures with **L1** and **L2**. Different multipliers of the stated stoichiometry (above the plot) are shown as columns in (D), and a bee-swarm spread is applied in the *x* axis position to avoid overlap. The lowest energy is highlighted by a black circle.

(E) Lowest-energy structures from each stoichiometry study (including *cis*-Pd_2**L1**$_2$**L2**$_2$); lines mark position in (D); bead colors as in (C).

is a first-step approximation for large-scale structure prediction that does not consider the building block fluctuations due to environmental and assembly effects. We explore the strain energy per building block (E_b), arising from the placement of these toy-building blocks into arbitrary cage graphs (Section S6.3). For **L1** + **L2**, our method automatically builds 489 systems with stoichiometry 3:2:4 (multiplier of 1) and 531 with stoichiometry 1:1:1 (multipliers of 1, 2, and 3). Figure 2D shows that the lowest-energy topology for **L1** and **L2** is a double-walled isosceles triangle topology with an arrangement of the building blocks as expected from the experimental results. With a 1:1:1 ratio, we see that a double-walled triangle with a non-symmetric arrangement of building blocks (one edge bridged by two different ligands) is also the lowest in energy, however, still highly strained. The common $M_2L_2L'_2$ structure is shown to be also of rather high energy for the **L1** + **L2** combination. This structure prediction approach agrees with the experimental data derived above and provides a platform for further exploration.

One key benefit of the toy-model approach is that we can scan multiple "configurations" or "mappings" between models to derive structure-property relationships. First, we performed a one-dimensional scan of the stability of the $M_3L_4L'_2$ structure from the **L1** parameters *aa*, *dd*, *de*, *bac*, and *dde* (Figure S96; as we focus only on one topology, we performed more costly geometry optimizations in this case). From there, we found that only the angles *bac* and *dde* led to significant changes in energy. Hence, we scanned these parameters (and others; Section S6) in two dimensions. The angle *bac* directly determines the ligand binder angles, while *dde* has this effect by altering the position of the rotatable pyridine ring. From this analysis, we see that the range of stable *bac* angles is limited to around 110°–130° (depending on the variable on the other dimension). We also see a twisting of the twistable ligand in these maps (Figures 3B and S98), but the $M_3L_4L'_2$ topology cannot support the convex binding mode seen in the other examples.

To further support the robustness of the experimental and computational approaches, we employed another chiral ligand **L1b** (*R,R* enantiomer) that upon combination with **L2** yielded the same type of ring with the formula Pd_3**L1b**$_2$**L2**$_4$. Indeed, **L1b** and **L1** are roughly similar in shape concerning binding angles and distances (Figure S95); both align within the stable regions of the grid-based scan (Figures S95–S99). That a comparable structure is formed was confirmed by observing the same splitting in the ^{1}H NMR of the assembly, as well as by evident ROESY cross-peaks (Figures S59–S64). At the same time, high-resolution (HR)-ESI-MS shows only peaks corresponding to the expected species. Eventually, we obtained single crystals suitable for X-ray synchrotron diffraction from benzene vapor diffusion in acetonitrile (Figures 3D, S105, and

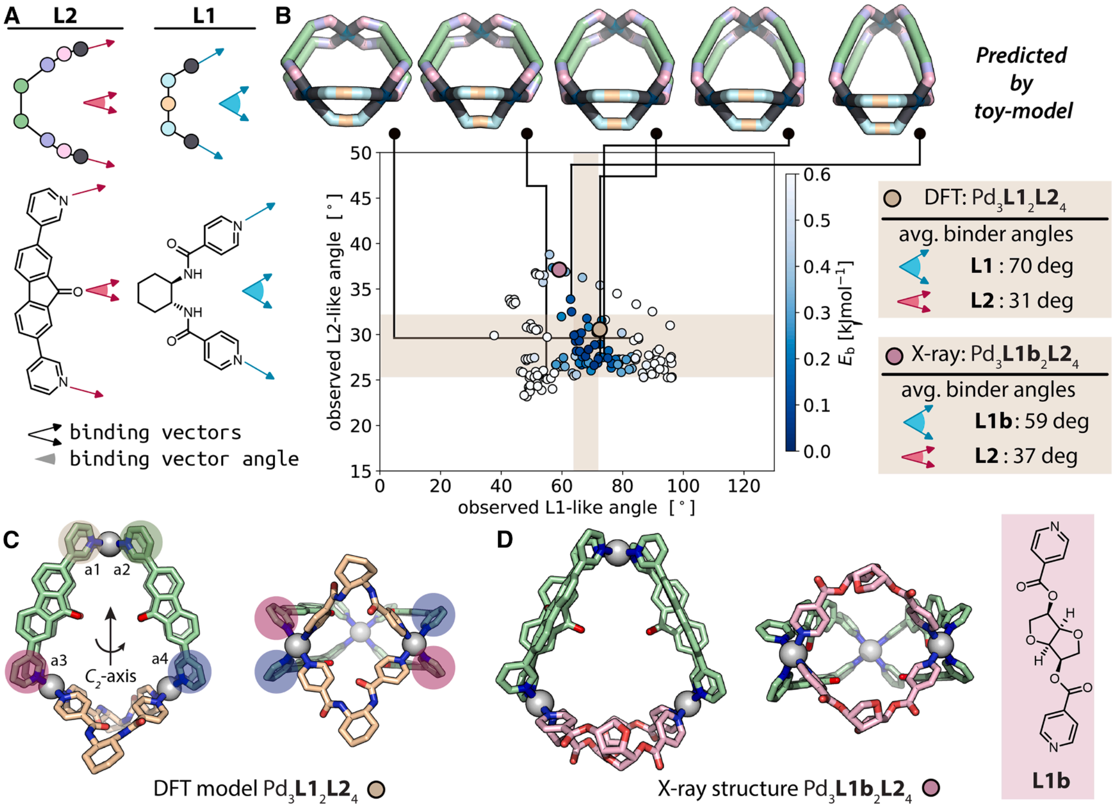

Figure 3. Geometric parameters extracted from toy model and comparison with DFT modeling and single-crystal X-ray structure

(A) Relationship between the binder-vector angles and the atomistic and toy models.

(B) A map of the measured **L1**-like and **L2**-like angles of toy-model cage structures obtained from a scan of the *bac* and *dde* angles. Beige regions highlight the limit of angles where stable structures are found (E_b < 0.1 kJ mol^{-1}). Some toy models covering this space (of various stability) are shown at the top. The parameters corresponding to the atomistic structures presented in (C) and (D) are highlighted in beige boxes and marked on the map to visualize the model adequation with experimental and higher computational data.

(C) Top and side view of DFT model (ωB97X-D/def2-SVP) of Pd_3**L1**$_2$**L2**$_4$, with the different chemical environments of **L2** highlighted.

(D) Top and side view of the X-ray structure of Pd_3**L1b**$_2$**L2**$_4$, with **L1b** structure shown in the pink box.

S106). The compound crystallizes in a monoclinic C_2 space group, being one of the 65 Sohncke space groups where chiral compounds can crystallize. In the obtained ring structure, the expected ligand arrangement can be observed with the two ligands **L1b** sitting on the same edge while the four ligands **L2** bridge to the third Pd(II). When considering that the fluorenone ligands are able to freely rotate in solution, the mentioned C_2 axis through the middle of the space between the two chiral ligands and the opposite Pd(II) center can be anticipated. In the X-ray structure, however, two fluorenone ligands on one side with respect to the ring plane are rotated by about 90° to this plane and face the backbones of their neighboring ligands, similar to what we previously observed in the solid-state structure of the Pd_3**L2**$_6$ homoleptic assembly. The binding angles between pyridines of the same **L2** range between 31.5° and 37.0°, while for **L1b**, the binding vectors are more divergent with angles of ~60°. This results in a cone-shaped structure with the two chiral ligands bulging slightly outward from the triangle. Based on this X-ray structure, we constructed a density functional theory (DFT) geometry-optimized model for Pd_3**L1**$_2$**L2**$_4$ and observed that both species are similar in shape (Figures 3C and S100). We stress, however, that while both **L1** and **L1b** take comparable positions in assemblies Pd_3**L1**$_2$**L2**$_4$ and Pd_3**L1b**$_2$**L2**$_4$, the edge occupied by **L1** (based on the Pd-Pd distance in the corresponding DFT model) measures about 85% of the respective Pd-Pd distance in the X-ray structure of the **L1b**-containing assembly (12.3 Å). A closer look at the structures reveals that ligand **L1**, having amide linkages installed in vicinal positions on the aliphatic ring, allows for H-bonding between the amides of both ligand arms, thus rather contracting the edge (and also bending ligands **L2** slightly inward), while **L1b**, carrying the donor arms in positions separated by three bonds on the aliphatic core (and featuring non-H-bonding esters instead of amides), possesses a more extended geometry. Similar structural features are also seen in the toy models.

Formation of a pseudo-tetrahedron by ABIs

In line with our strategy to obtain higher-nuclearity heteroleptic structures such as $Pd_4A_4B_4$ rings, saddles,[36] or tetrahedra,[37] we were curious to test the effect of using bulkier fluorene- or carbazole-type ligands in combination with **L1**. We thus expanded the scope of ligands by employing **L5**, featuring a

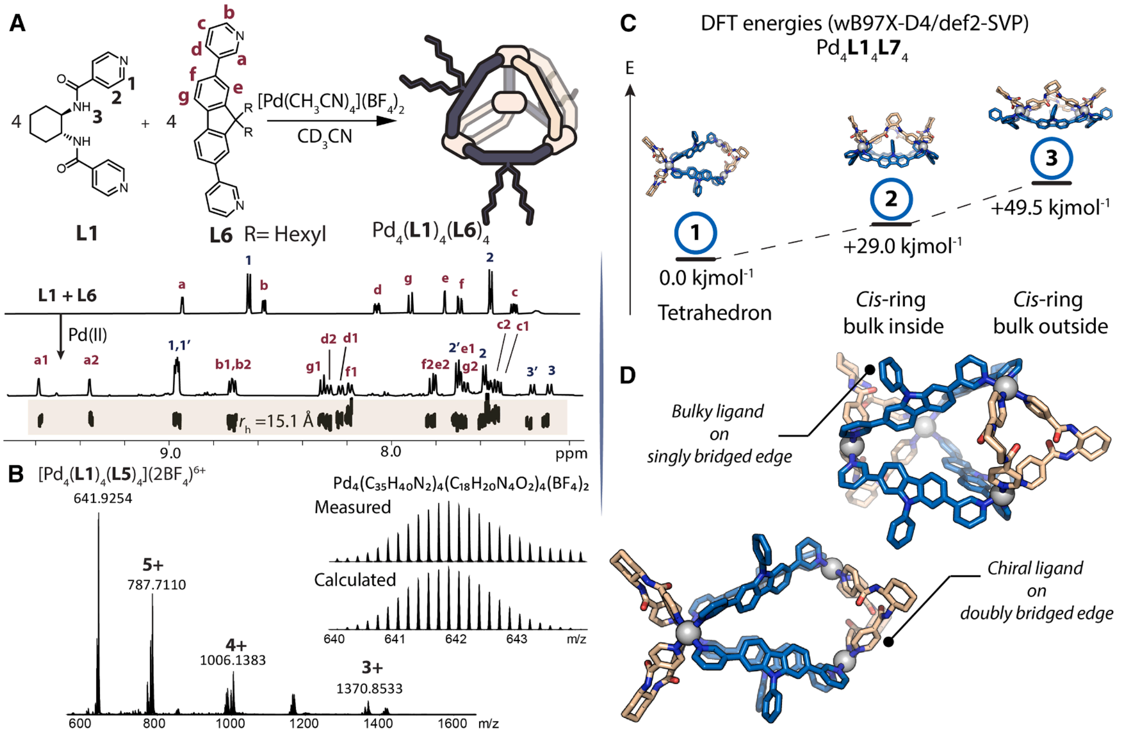

Figure 4. Assembly of a $Pd_4\mathbf{L1}_4\mathbf{L6}_4$ architecture and DFT modeling of the lowest-energy isomer for $Pd_4\mathbf{L1}_4\mathbf{L7}_4$

(A) Self-assembly of **L1** and **L6** with Pd(II) yields a $Pd_4\mathbf{L1}_4\mathbf{L6}_4$ tetrahedron. ^1H NMR (CD_3CN, 500 MHz) stack of a mixture of both ligands and after addition of Pd(II). Assignment and ^1H DOSY NMR trace are given on the spectra.

(B) HR-ESI-MS of an acetonitrile solution of $Pd_4\mathbf{L1}_4\mathbf{L6}_4$. The inset shows measured and calculated isotopic patterns.

(C) Energy diagram of three plausible $Pd_4\mathbf{L1}_4\mathbf{L7}_4$ isomers obtained through DFT modeling (ωB97X-D/def2-SVP).

(D) Side and top views of the $Pd_4\mathbf{L1}_4\mathbf{L7}_4$ lowest-energy structure.

slightly more sterically demanding structure, as well as **L6** and **L7**, comprising significantly larger steric hindrance.

When combined in a 1:1:1 ratio with a Pd(II) source, **L1** and **L5**–**L7** lead to the emergence of new ^1H NMR signals that do not correspond to the respective homoleptic species (Figures S31–S58). As the three obtained assembly products share the same characteristics, we will only describe exemplary cases. For the combination of **L1** with **L6**, a DOSY experiment indicated that all the signals belong to the same species with a hydrodynamic radius r_H = 15.1 Å (Figure 4A). In this assembly, all protons from ligands **L1** and **L6** split into two sets of signals of equal intensities, indicating a higher symmetry than the isosceles triangular rings introduced above. Further, ESI-MS analysis revealed a stoichiometry of $[Pd_4\mathbf{L1}_4\mathbf{L6}_4{+}n\ BF_4]^{(4-n)+}$ (n = 2–5; Figure 4B). This sum formula would allow for several possible topologies, including a rectangular or cone-shaped four-ring (or saddle) or a doubly bridged tetrahedron. NOESY analysis provided a first insight into the structure. The set of cross-peaks between Ha and Hf, as well as Hd and He, evidences an **L6** orientation where the backbone substituent is pointing in the opposite direction to the coordination vectors. This is compatible with a binding angle of ~90° and therefore should favor the formation of tetrahedral or octahedral assemblies. At the same time, cross-peaks between the pyridine protons of both **L1** (H1) and **L6** (Ha,b) confirm the *cis*-arrangement of the ligands per square-planar Pd(II) center. Finally, the lack of cross-peaks between **L6** alkyl chain protons and either signals from **L1** or from the second set belonging to **L6** is evidence of a topology where the fluorene-based ligands singly bridge edges between neighboring Pd(II) centers, thus supporting the formation of an heteroleptic pseudo-tetrahedron. As we could not obtain single crystals suitable for X-ray diffraction analysis, we employed modeling (GFN2-xTB/ALPB (acetonitrile) and DFT ωB97-D4/def2-SVP; Figure 4C) to support and better understand the structure (Figures S101 and S102). For this, we constructed the tetrahedron as well as tentative *cis*-rings, both with bulky substituents pointing inside or outside the cavity. We built the tetrahedron so that the bulky ligands occupy singly bridged edges, while the chiral ones sit in pairs on the remaining ones. This arrangement was previously observed for other $Pd_4A_4C_4$ heteroleptic tetrahedral Pd(II)-cages[37] and is supported by 2D NMR analysis, with the notable exception that the chirality of the here used ligand **L1** leads to an additional splitting of the signal sets of **L6**. To avoid lengthy calculations because of alkyl chain flexibility, but still considering the effect of the backbone bulk, we modeled structural isomers of related, phenyl-substituted compound $Pd_4\mathbf{L1}_4\mathbf{L7}_4$. Indeed, the calculations indicate that the tetrahedral assembly is lower in energy as compared with its ring analogs, with a respective difference of 29.0 kJ mol^{-1} for the ring with the bulk inside and 49.5 kJ mol^{-1} for the least favored structure with bulk pointing

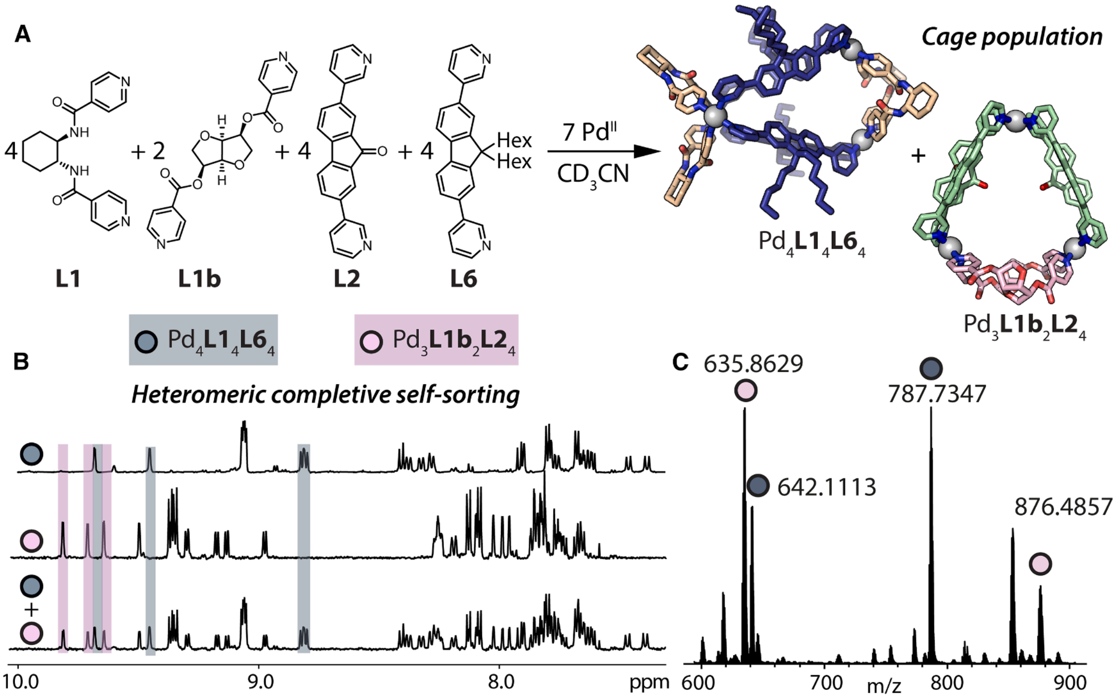

Figure 5. Formation of a cage population from four different building blocks through heteromeric narcissistic self-sorting

(A) The one-pot, yet orthogonal, self-assembly of **L1b**, **L1**, **L2**, and **L6** with Pd(II) cations in a 2:4:4:4 ratio leads to the concomitant formation of a Pd$_4$**L1**$_4$**L6**$_4$ pseudo-tetrahedron and a Pd$_3$**L1b**$_2$**L2**$_4$ ring.

(B) ^{1}H NMR (CD$_3$CN, 500 MHz) stack of (top, dark blue highlighted) Pd$_4$**L1**$_4$**L6**$_4$, (middle, pink) Pd$_3$**L1b**$_2$**L2**$_4$, and (bottom) the outcome of the heteromeric narcissistic self-sorting, leading to a defined cage population.

(C) HR-ESI-MS of the cage population showing the formation of the two separate species, marked by blue and pink dots.

outside (Figure 4C). These results match our 2D NMR analysis (Figures S31–S58) and are in accordance with the DOSY-derived hydrodynamic radius (Figure 4B). The ABIs prevent the formation of ring structures in which bulky ligands would sterically clash if they were arranged next to each other on the same edges bridging neighboring Pd(II) centers. These interactions enable the formation of tetranuclear heteroleptic pseudo-tetrahedra in all cases when **L5**–**L7** are combined with **L1**.

It is worth mentioning that the methyl groups in **L5** represent the borderline case to direct the formation toward one or the other structure. As previously mentioned, the bulky substituents on **L6** and **L7** lead to the formation of homoleptic Pd$_6$L$_{12}$ octahedral species. Therefore, it is not surprising to obtain the tetrahedron when they are combined with **L1**. Homoleptic assembly of **L5** with Pd(II) cations yields a mixture of Pd$_4$L$_8$ and P$_3$L$_6$ species analogous to those obtained with **L2**. However, the slight increase in backbone steric hindrance from **L2** (C=O) to **L5** (C(CH$_3$)$_2$) is enough to dictate the formation of a Pd$_4$**L1**$_4$**L5**$_4$ heteroleptic tetrahedron rather than an isosceles triangular ring as observed for **L2**.

Formation of cage populations

We recently reported the formation of heteroleptic cage populations through *heteromeric completive* self-sorting, which allowed us to observe orthogonally coexisting dinuclear Pd(II)-based structures.[29] This was quickly followed by a report from Chand and coworkers, where they observed the coexistence of heteroleptic species obtained from unsymmetrical ligands,[27] as well as a further paper where we reported guest segregation in a multi-cage heteromeric system.[28] Above, we demonstrated that **L1** and **L1b** both associate with **L2** to form an unprecedented Pd$_3$A$_2$B$_4$-type ring motif. We also observed that **L1b**, differing from **L1** by its chemically distinct backbone structure, does not readily assemble with any of the other **L3**–**L7** ligands. We were therefore curious about the possibility of orthogonally assembling multiple species in the same reaction vessel (Figures S85–S88). First, we mixed **L1**, **L1b**, and **L2** with Pd(II) in a 2:2:8:6 ratio in acetonitrile. After stirring the solution overnight, we observed the concomitant formation of the two rings Pd$_3$**L1**$_2$**L2**$_4$ and Pd$_3$**L1b**$_2$**L2**$_4$, independently coexisting in the same mixture. While the two chiral ligands are structurally similar, subtle differences lead to clean narcissistic sorting of the two rings without shuffling of components. Even more interesting observations were made by mixing the four different ligands **L1**, **L1b**, **L2**, and **L6** in a 4:2:4:4 ratio with Pd(II) (Figure 5A). Here, it was possible to obtain a population composed of the Pd$_4$**L1**$_2$**L6**$_4$ tetrahedron and the Pd$_3$**L1b**$_2$**L2**$_4$ ring, as confirmed by the perfect overlay of the ^{1}H NMR traces of the two separate assemblies, as well as the identification of these assemblies as the major components of the population by ESI-MS (Figures 5B and 5C). We phrase this heteromeric narcissistic self-sorting. The outcome here is not trivial as we

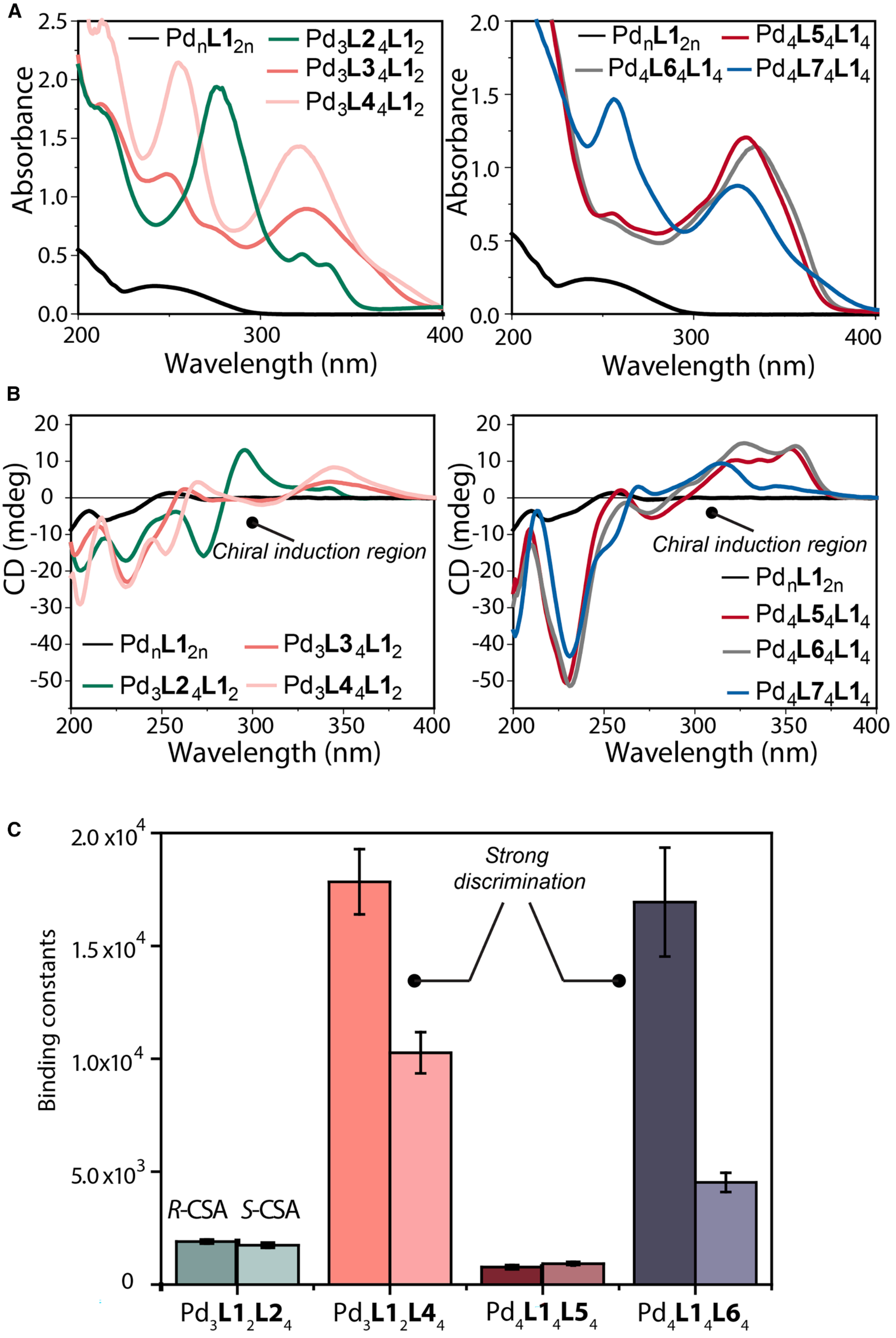

(legend on next page)

also reported before that **L2** and **L6** can associate into an heteroleptic tetrahedron $\mathrm{Pd_4}\mathbf{L2}_4\mathbf{L6}_4$.[37] Because **L1b** can only pair with **L2**, forming $\mathrm{Pd_3}\mathbf{L1b}_2\mathbf{L2}_4$ as the assembly of smallest possible nuclearity, it depletes the mixture from this ligand in a way that the remaining **L1** and **L6** must associate into $\mathrm{Pd_4}\mathbf{L1}_4\mathbf{L6}_4$.

No other species, i.e., $\mathrm{Pd_4}\mathbf{L2}_4\mathbf{L6}_4$ or $\mathrm{Pd_3}\mathbf{L1}_2\mathbf{L2}_4$, were observed, indicative of a highly selective sorting process. We assume that subtle geometrical differences, combined with entropic factors and the given stoichiometry, are at the origin of a precise sorting outcome of the ligands into a defined population, rather than the formation of a statistical mess. This now not only extends the concept of gaining control over cage populations to *higher*-nuclearity assemblies but also to coexisting heteroleptic species with *different* nuclearities and chiral building blocks. Eventually it is worth noting that in reference to our previously reported integratively self-sorted $\mathrm{Pd_2ABCD}$ cage,[38] this is the first observation of combining four different building blocks leading to two coexisting structures, each based on two distinguishable ligands.

Intra-assembly chiral induction

In light of the use of a homochiral ligand, we asked whether its chiral information is transmitted onto the region occupied by the fluorene or carbazole-type backbones, detectable by chiroptical spectroscopies.[50] Consequently, we proceeded with the (chiro)optical characterization of these rings and cages (Figures 6A, 6B, S89, and S90). As previously documented, chiral ligand **L1** only exhibits weak absorbance below 300 nm, characterized by a broad band centered at 250 nm. For the rings (Figure 6A, left), $\mathrm{Pd_3}\mathbf{L1}_2\mathbf{L2}_4$ displayed a strong absorption maximum at 275 nm, accompanied by smaller absorption bands centered at 325 and 335 nm, and a weaker broad band around 400 nm, characteristic of the fluorenone moiety. Notably, these latter three bands resided within a spectral region where **L1** exhibits no absorption, thereby facilitating the clear attribution of their origin to **L2**. $\mathrm{Pd_3}\mathbf{L1}_2\mathbf{L3}_4$ and $\mathrm{Pd_3}\mathbf{L1}_2\mathbf{L4}_4$ similarly showed absorption bands at 250 and 255 nm, respectively, which therefore overlap with the absorption of **L1**. However, both structures revealed a second absorption maximum with $\lambda > 300$ nm with the bands centered at 325 and 320 nm. The latter features arise from the sole contribution of the carbazole-based cores of **L3** and **L4**. A similar trend is observed for the tetrahedral assemblies (Figure 6A, right) obtained from **L5**, **L6**, and **L7**, with one band overlapping with **L1** around 255 nm and the second distinctive band centered at 330, 335, and 325 nm, respectively.

L1 in enantiopure form has previously been shown to impart chirality onto the overall structure of a heteroleptic $\mathrm{Pd_2A_2B_2}$ cage, yielding a CD signature for the originally achiral counter ligand.[50] We therefore expected similar observations for the herein studied higher-nuclearity rings and tetrahedra (Figure S89). Indeed, the characteristic UV-vis absorptions of the achiral chromophores occurred as features in the CD spectra above 300 nm for all examined species (Figure 6B). These results validated that the chirality of **L1** is imparted onto the overall assembly and thus to the counter ligands **L2**–**L7**. This chirality transfer was further probed for assembly $\mathrm{Pd_3}\mathbf{L1}_2\mathbf{L2}_4$ by CPL spectroscopy, as **L2** retained some luminescent properties even after coordination to Pd(II). Given that **L1** is not luminescent, any CPL signals would show that the initially achiral fluorenone cores have been brought into a chiral arrangement. Although the measured luminescence was relatively weak, a CPL signal with a low dissymmetry factor $g_{\mathrm{lum}} = 10^{-4}$ centered at 505 nm could be detected (Figure S90), a typical region of emission for the fluorenone chromophore (supplemental information). In contrast, for all other assemblies, the luminescence was entirely quenched.

Chiral guest discrimination

As we obtained a family of chiral assemblies (containing the *R,R* enantiomers of the respective ligands) with an accessible cavity, we examined whether they can differentiate between two enantiomers of a chiral guest (Figure 6C). We studied the binding of *R*/*S*-camphor sulfonate inside the rings and tetrahedra by NMR-based titrations (Figures S65–S84). For $\mathrm{Pd_3}\mathbf{L1}_2\mathbf{L2}_4$, guest addition resulted in a shift of inward pointing protons, indicating binding inside the host cavity. However, the 1:1 binding constants of the two enantiomers *R* and *S* were both small and comparable, with values of 1,900 and 1,742 $\mathrm{M^{-1}}$. Binding was also supported by ESI-MS (supplemental information). On the other hand, $\mathrm{Pd_3}\mathbf{L1}_2\mathbf{L4}_4$ led to a chiral discrimination with a factor of 1.7 between *R* and S and binding constants 10 times higher than those for $\mathrm{Pd_3}\mathbf{L1}_2\mathbf{L2}_4$,with 17,839 and 10,268 $\mathrm{M^{-1}}$, respectively. This discrimination value is rather good and in line with literature-reported examples.[53] The differing binding abilities of these rings may relate to the inward pointing groups. In $\mathrm{Pd_3}\mathbf{L1}_2\mathbf{L2}_4$, four carbonyl moieties are directed with their negative partial charges inside the cavity (disfavoring binding of the anionic guest), while in $\mathrm{Pd_3}\mathbf{L1}_2\mathbf{L4}_4$ four methyl groups occupy those positions (probably favoring guest binding by enhancing the hydrophobic character of the cavity). Noteworthy, we have recently described a discrimination factor close to 3 for another chiral Pd-based host binding the same guest.[54] For tetrahedron $\mathrm{Pd_4}\mathbf{L1}_4\mathbf{L5}_4$, NMR titration yielded binding constants of 772 and 922 $\mathrm{M^{-1}}$ for *R* and *S* camphor sulfonate. In the case of $\mathrm{Pd_4}\mathbf{L1}_4\mathbf{L6}_4$, we also observed shifting, accompanied by broadening, of some proton signals. Here, the binding constant for the *R* enantiomer was determined to be 16,938 $\mathrm{M^{-1}}$, while the one for the *S* enantiomer is only 4,523 $\mathrm{M^{-1}}$, leading to a remarkable discrimination factor of 3.75. As observed in the crystal structure of a similar tetrahedron[37] and the model in Figure 5, the hexyl chains of the ligands on the singly

Figure 6. Chiral induction and guest discrimination

(A) UV-vis spectra overlay of (left) the different $\mathrm{Pd_3}\mathbf{L1}_2\mathbf{Lx}_4$ (x = 2, 3, 4) rings and (right) $\mathrm{Pd_4}\mathbf{L1}_4\mathbf{Lx}_4$ (x = 5, 6, 7) tetrahedra.

(B) Overlay of CD spectra of (left) the different $\mathrm{Pd_3}\mathbf{L1}_2\mathbf{Lx}_4$ rings and (right) $\mathrm{Pd_4}\mathbf{L1}_4\mathbf{Lx}_4$ tetrahedra. The intra-assembly chiral induction is observable through CD bands present in regions where only ligands **L2**–**L7** are absorbing.

(C) Bar chart comparing the binding constants for *R* and *S* camphor sulfonate among the different hosts. Strong discrimination is observed for *R*,*R*-$\mathrm{Pd_3}\mathbf{L1}_2\mathbf{L4}_4$ and *R*,*R*-$\mathrm{Pd_4}\mathbf{L1}_4\mathbf{L6}_4$ along with high binding constants. Error bars represent the standard fitting error estimations by the bindfit software.

bridged edges in Pd_4**L1**$_4$**L6**$_4$ partially cover the faces of the tetrahedron, leading to a better enclosed cavity, as compared with Pd_4**L1**$_4$**L5**$_4$, and hence stronger guest binding. Guest addition to Pd_3**L1**$_2$**L3**$_4$ and Pd_4**L1**$_4$**L7**$_4$ resulted in turbid solutions and precipitation, and it was therefore not possible to determine binding constants. All results are summarized in Figure 6C.

Conclusions

Based on readily accessible chiral and luminescent ligands, a family of heteroleptic metallosupramolecular structures with nuclearities of three and four was obtained, and among them were the first $Pd_3A_2B_4$-type structures of isosceles triangular ring topology. A sequential increase in steric bulk results in ABIs, leading to the formation of heteroleptic pseudo-tetrahedra $Pd_4A_4C_4$. Experimentally observed assembly results could be rationalized and supported using low-cost computational toy models. Based on only some key structural and geometrical parameters of the building blocks, this algorithm affords the prediction of the most stable assemblies, hence considerably advancing the rational and guided design of low-symmetry coordination cages. While the software is freely available, improvements to the structure prediction algorithm are currently in progress. We further demonstrated the controlled formation of cage populations through heteromeric narcissistic self-sorting, where discernable species coexist orthogonally. This extends the toolbox of cage-based self-sorting schemes to chiral assemblies as well as higher-nuclearity species, opening new avenues to create structural complexity and functional applicability. We further showed that the chirality of one ligand is transmitted to the overall assembly, resulting in chiral induction on otherwise non-chiral chromophores. On the other hand, formed hosts could encapsulate and discriminate the enantiomers of a small chiral guest with selectivity factors up to 3.75.

Our study demonstrated how a collection of a few chemically simple but meticulously designed building blocks can lead to structurally complex assemblies and self-sorted mixtures, thus progressing the control over tailored nano architectures. We just started to apply the herein reported compounds and principles in dynamic systems with life-like properties, capable of dissipative transient species formation, competition in populations held under restrictive supply of limiting components, and molecular information propagation. They may further find application in chemical separation tasks, catalysis under confinement, and porous materials.

METHODS

All the experimental procedures and data are detailed in the supplemental information.

RESOURCE AVAILABILITY

Lead contact

Requests for further information and resources should be directed to and will be fulfilled by the lead contact Prof. Guido H. Clever (guido.clever@tu-dortmund.de).

Materials availability

Synthetic procedures, NMR, MS, single-crystal X-ray diffraction (SCXRD) results, and calculation data are included in the supplemental information PDF file. Data sets CCDC: 2429500, 2429501, 2406153 contain the crystallographic data.

Data and code availability

Software is freely available at https://github.com/andrewtarzia/starships (https://zenodo.org/records/15205588), with minimal model data available at https://zenodo.org/records/14909754 and explorable at https://cgmodels.readthedocs.io/en/latest/starships_mar2025.html.

ACKNOWLEDGMENTS

This work was supported by the Deutsche Forschungs-gemeinschaft (DFG) through GRK2376 (“Confinement-Controlled Chemistry,” project number 331085229) and under Germany’s Excellence Strategy EXC2033, project number 390677874 (“RESOLV”). J.T. and H.L. acknowledge the National Research Foundation of Korea (NRF) grants funded by the Korea government (MSIT) (nos. RS-2024-00348192 and RS-2021-NR061709) and Global-Learning & Academic Research Institution for Master’s, PhD students, and Postdocs (LAMP) Program (no. RS-2024-00442775). A.T. acknowledges the European Union – Next Generation EU, Mission 4 Component 1 CUP E13C22002930006. G.M.P. acknowledges funding received from the ERC under the European Union Horizon 2020 research and innovation program (grant agreement no. 818776, DYNAPOL). Diffraction data of Pd_3**L1b**$_2$**L2**$_4$ and Pd_6**L7**$_{12}$ were collected at PETRA III and processed on the Maxwell computational resources operated at DESY (Hamburg, Germany), a member of the Helmholtz Association (HGF). We thank Julian J. Holstein for organizing the synchrotron beamtime and for help with sample preparation and data collection; Guillaume Pompidor, Helena Taberman, and Eva Crosas for assistance at synchrotron beamline P11 (I-20231259, I-20200916, STP-20010307); and DESY user office for travel funds.

AUTHOR CONTRIBUTIONS

E.B., J.T., and G.H.C. conceived the project. E.B. and J.T. performed the experiments and analyzed the data. A.T. created the toy model and performed calculations. A.J. and M.W.H. provided the chiral ligands. H.L. and J.T. refined the X-ray structures. E.B., J.T., and A.T. drafted the manuscript, revised by G.H.C., M.W.H., and G.M.P. All the authors have seen the manuscript and agreed on its content.

DECLARATION OF INTERESTS

The authors declare no competing interests.

SUPPLEMENTAL INFORMATION

Supplemental information can be found online at https://doi.org/10.1016/j.chempr.2025.102780.

Received: May 26, 2025
Revised: July 28, 2025
Accepted: September 12, 2025
Published: October 15, 2025

REFERENCES

1. Grommet, A.B., Bolliger, J.L., Browne, C., and Nitschke, J.R. (2015). A Triphasic Sorting System: Coordination Cages in Ionic Liquids. Angew. Chem. Int. Ed. Engl. *54*, 15100–15104. https://doi.org/10.1002/anie.201505774.
2. Zhang, W.-Y., Lin, Y.-J., Han, Y.-F., and Jin, G.-X. (2016). Facile Separation of Regioisomeric Compounds by a Heteronuclear Organometallic Capsule. J. Am. Chem. Soc. *138*, 10700–10707. https://doi.org/10.1021/jacs.6b06622.
3. Ryan, H.P., Haynes, C.J.E., Smith, A., Grommet, A.B., and Nitschke, J.R. (2021). Guest Encapsulation within Surface-Adsorbed Self-Assembled Cages. Adv. Mater. *33*, e2004192. https://doi.org/10.1002/adma.202004192.

4. Zhang, D., Ronson, T.K., Zou, Y.-Q., and Nitschke, J.R. (2021). Metal–organic cages for molecular separations. Nat. Rev. Chem. *5*, 168–182. https://doi.org/10.1038/s41570-020-00246-1.
5. García-Simón, C., Garcia-Borràs, M., Gómez, L., Parella, T., Osuna, S., Juanhuix, J., Imaz, I., Maspoch, D., Costas, M., and Ribas, X. (2014). Sponge-like molecular cage for purification of fullerenes. Nat. Commun. *5*, 5557. https://doi.org/10.1038/ncomms6557.
6. Iizuka, K., Takezawa, H., and Fujita, M. (2024). Template and Solid-State-Assisted Assembly of an M_9L_6 Expanded Coordination Cage for Medium-Sized Molecule Encapsulation. J. Am. Chem. Soc. *146*, 32311–32316. https://doi.org/10.1021/jacs.4c14509.
7. Cullen, W., Metherell, A.J., Wragg, A.B., Taylor, C.G.P., Williams, N.H., and Ward, M.D. (2018). Catalysis in a Cationic Coordination Cage Using a Cavity-Bound Guest and Surface-Bound Anions: Inhibition, Activation, and Autocatalysis. J. Am. Chem. Soc. *140*, 2821–2828. https://doi.org/10.1021/jacs.7b11334.
8. Mozaceanu, C., Taylor, C.G.P., Piper, J.R., Argent, S.P., and Ward, M.D. (2020). Catalysis of an Aldol Condensation Using a Coordination Cage. Chemistry *2*, 22–32. https://doi.org/10.3390/chemistry2010004.
9. Xue, Y., Hang, X., Ding, J., Li, B., Zhu, R., Pang, H., and Xu, Q. (2021). Catalysis within coordination cages. Coord. Chem. Rev. *430*, 213656. https://doi.org/10.1016/j.ccr.2020.213656.
10. Chen, J., Wu, X., Huang, S., Yang, J., Lu, Y.-L., Jiao, Z., and Su, C.-Y. (2024). Catalytic Enantioselective Cycloaddition Transformation of Tricyclic Arenes Enabled by a Dual-Role Chiral Cage-Reactor. ACS Catal. *14*, 3733–3741. https://doi.org/10.1021/acscatal.3c06361.
11. Piskorz, T.K., Martí-Centelles, V., Spicer, R.L., Duarte, F., and Lusby, P.J. (2023). Picking the lock of coordination cage catalysis. Chem. Sci. *14*, 11300–11331. https://doi.org/10.1039/d3sc02586a.
12. Spicer, R.L., O'Connor, H.M., Ben-Tal, Y., Zhou, H., Boaler, P.J., Milne, F.C., Brechin, E.K., Lloyd-Jones, G.C., and Lusby, P.J. (2023). Exo-cage catalysis and initiation derived from photo-activating host-guest encapsulation. Chem. Sci. *14*, 14140–14145. https://doi.org/10.1039/d3sc04877b.
13. Takezawa, H., Iizuka, K., and Fujita, M. (2024). Selective Synthesis and Functionalization of an Acyclic Methylene-Bridged-Arene Trimer in a Cage. Angew. Chem. Int. Ed. Engl. *63*, e202319140. https://doi.org/10.1002/anie.202319140.
14. Iizuka, K., Takezawa, H., and Fujita, M. (2023). Chemical Site-Differentiation of Calix[4]arenes through Enforced Conformations by Confinement in a Cage. J. Am. Chem. Soc. *145*, 25971–25975. https://doi.org/10.1021/jacs.3c10720.
15. Tateishi, T., Yoshimura, M., Tokuda, S., Matsuda, F., Fujita, D., and Furukawa, S. (2022). Coordination/metal–organic cages inside out. Coord. Chem. Rev. *467*, 214612. https://doi.org/10.1016/j.ccr.2022.214612.
16. Liu, C., Zhang, Y., and An, Q. (2021). Functional Material Systems Based on Soft Cages. Chem. Asian J. *16*, 1198–1215. https://doi.org/10.1002/asia.202100178.
17. Hosono, N., and Kitagawa, S. (2018). Modular Design of Porous Soft Materials via Self-Organization of Metal–Organic Cages. Acc. Chem. Res. *51*, 2437–2446. https://doi.org/10.1021/acs.accounts.8b00361.
18. Pullen, S., Tessarolo, J., and Clever, G.H. (2021). Increasing structural and functional complexity in self-assembled coordination cages. Chem. Sci. *12*, 7269–7293. https://doi.org/10.1039/d1sc01226f.
19. Lewis, J.E.M. (2023). Developing sophisticated microenvironments in metal-organic cages. Trends Chem. *5*, 717–719. https://doi.org/10.1016/j.trechm.2023.06.003.
20. Lewis, J.E.M. (2022). Molecular engineering of confined space in metal–organic cages. Chem. Commun. (Camb) *58*, 13873–13886. https://doi.org/10.1039/d2cc05560k.
21. Percástegui, E.G., Ronson, T.K., and Nitschke, J.R. (2020). Design and Applications of Water-Soluble Coordination Cages. Chem. Rev. *120*, 13480–13544. https://doi.org/10.1021/acs.chemrev.0c00672.
22. Tarzia, A., Shan, W., Posligua, V., Cox, C.J.T., Male, L., Egleston, B.D., Greenaway, R.L., Jelfs, K.E., and Lewis, J.E.M. (2025). A combined experimental and computational exploration of heteroleptic cis-Pd2L2L'2 coordination cages through geometric complementarity. Chemistry *31*, e202403336. https://doi.org/10.1002/chem.202403336.
23. Wu, K., Zhang, B., Drechsler, C., Holstein, J.J., and Clever, G.H. (2021). Backbone-Bridging Promotes Diversity in Heteroleptic Cages. Angew. Chem. Int. Ed. Engl. *60*, 6403–6407. https://doi.org/10.1002/anie.202012425.
24. Li, R.-J., de Montmollin, J., Fadaei-Tirani, F., Scopelliti, R., and Severin, K. (2023). Construction of Pd-based coordination cages with three geometrically distinct ligands. Dalton Trans. *52*, 6451–6456. https://doi.org/10.1039/d3dt00248a.
25. Liu, Y., Liao, S.H., Dai, W.T., Bai, Q., Lu, S., Wang, H., Li, X., Zhang, Z., Wang, P., Lu, W., et al. (2023). Controlled Construction of Heteroleptic $[Pd_2(LA)_2(LB)(LC)]^{4+}$ Cages: A Facile Approach for Site-Selective endo-Functionalization of Supramolecular Cavities. Angew. Chem. Int. Ed. Engl. *62*, e202217215. https://doi.org/10.1002/anie.202217215.
26. Chen, B., Holstein, J.J., Platzek, A., Schneider, L., Wu, K., and Clever, G.H. (2022). Cooperativity of steric bulk and H-bonding in coordination sphere engineering: heteroleptic Pd(II) cages and bowls by design. Chem. Sci. *13*, 1829–1834. https://doi.org/10.1039/d1sc06931d.
27. Parbin, M., Sivalingam, V., and Chand, D.K. (2024). Highly Anisotropic Pd2Lab2Lcc2 and $Pd_2Lab_2Lcd_2$ Type Cages by Heteromeric Completive Self-Sorting. Angew. Chem. Int. Ed. Engl. *63*, e202410219. https://doi.org/10.1002/anie.202410219.
28. Benchimol, E., Rivoli, A., Kabiri, M., Zhang, B., Holstein, J.J., Ballester, P., and Clever, G.H. (2025). Guest Segregation in Heteromeric Multicage Systems. J. Am. Chem. Soc. *147*, 3823–3829. https://doi.org/10.1021/jacs.4c16971.
29. Benchimol, E., Regeni, I., Zhang, B., Kabiri, M., Holstein, J.J., and Clever, G.H. (2024). Heteromeric Completive Self-Sorting in Coordination Cage Systems. J. Am. Chem. Soc. *146*, 6905–6911. https://doi.org/10.1021/jacs.3c14168.
30. Bloch, W.M., Abe, Y., Holstein, J.J., Wandtke, C.M., Dittrich, B., and Clever, G.H. (2016). Geometric Complementarity in Assembly and Guest Recognition of a Bent Heterolepticcis-$[Pd_2LA_2LB_2]$ Coordination Cage. J. Am. Chem. Soc. *138*, 13750–13755. https://doi.org/10.1021/jacs.6b08694.
31. Bloch, W.M., Holstein, J.J., Hiller, W., and Clever, G.H. (2017). Morphological Control of Heteroleptic cis- and trans-$Pd_2L_2L'_2$ Cages. Angew. Chem. Int. Ed. Engl. *56*, 8285–8289. https://doi.org/10.1002/anie.201702573.
32. Li, J.-R., and Zhou, H.-C. (2010). Bridging-ligand-substitution strategy for the preparation of metal–organic polyhedra. Nat. Chem. *2*, 893–898. https://doi.org/10.1038/nchem.803.
33. Sun, Q.F., Sato, S., and Fujita, M. (2014). An $M_{12}(L1)_{12}(L2)_{12}$ Cantellated Tetrahedron: A Case Study on Mixed-Ligand Self-Assembly. Angew. Chem. Int. Ed. Engl. *53*, 13510–13513. https://doi.org/10.1002/anie.201408652.
34. Chen, B., Holstein, J.J., Horiuchi, S., Hiller, W.G., and Clever, G.H. (2019). Pd(II) Coordination Sphere Engineering: Pyridine Cages, Quinoline Bowls, and Heteroleptic Pills Binding One or Two Fullerenes. J. Am. Chem. Soc. *141*, 8907–8913. https://doi.org/10.1021/jacs.9b02207.
35. Molinska, P., Tarzia, A., Male, L., Jelfs, K.E., and Lewis, J.E.M. (2023). Diastereoselective Self-Assembly of Low-Symmetry Pd_nL_{2n} Nanocages through Coordination-Sphere Engineering. Angew. Chem. Int. Ed. Engl. *62*, e202315451. https://doi.org/10.1002/anie.202315451.
36. Ebbert, K.E., Benchimol, E., Platzek, A., Drechsler, C., Openy, J., Hasegawa, S., Holstein, J.J., and Clever, G.H. (2024). Ring-Size Control and Guest-Induced Circularly Polarized Luminescence in Heteroleptic $Pd_3A_3B_3$ and $Pd_4A_4B_4$ Assemblies. Angew. Chem. Int. Ed. Engl. *63*, e202413323. https://doi.org/10.1002/anie.202413323.
37. Tessarolo, J., Lee, H., Sakuda, E., Umakoshi, K., and Clever, G.H. (2021). Integrative Assembly of Heteroleptic Tetrahedra Controlled by Backbone

Steric Bulk. J. Am. Chem. Soc. *143*, 6339–6344. https://doi.org/10.1021/jacs.1c01931.

38. Wu, K., Benchimol, E., Baksi, A., and Clever, G.H. (2024). Non-statistical assembly of multicomponent [Pd_2ABCD] cages. Nat. Chem. *16*, 584–591. https://doi.org/10.1038/s41557-023-01415-7.
39. Abe, T., Sanada, N., Takeuchi, K., Okazawa, A., and Hiraoka, S. (2023). Assembly of Six Types of Heteroleptic Pd_2L_4 Cages under Kinetic Control. J. Am. Chem. Soc. *145*, 28061–28074. https://doi.org/10.1021/jacs.3c09359.
40. Preston, D., and Evans, J.D. (2023). A Lantern-Shaped Pd(II) Cage Constructed from Four Different Low-Symmetry Ligands with Positional and Orientational Control: An Ancillary Pairings Approach. Angew. Chem. Int. Ed. Engl. *62*, e202314378. https://doi.org/10.1002/anie.202314378.
41. Poole, D.A., Bobylev, E.O., Mathew, S., and Reek, J.N.H. (2020). Topological prediction of palladium coordination cages. Chem. Sci. *11*, 12350–12357. https://doi.org/10.1039/d0sc03992f.
42. Young, T.A., Gheorghe, R., and Duarte, F. (2020). cgbind: A Python Module and Web App for Automated Metallocage Construction and Host–Guest Characterization. J. Chem. Inf. Model. *60*, 3546–3557. https://doi.org/10.1021/acs.jcim.0c00519.
43. Hay, B.P., and Firman, T.K. (2002). HostDesigner: A Program for the de Novo Structure-Based Design of Molecular Receptors with Binding Sites that Complement Metal Ion Guests. Inorg. Chem. *41*, 5502–5512. https://doi.org/10.1021/ic0202920.
44. Tarzia, A., Lewis, J.E.M., and Jelfs, K.E. (2021). High-Throughput Computational Evaluation of Low Symmetry Pd_2L_4 Cages to Aid in System Design. Angew. Chem. Int. Ed. Engl. *60*, 20879–20887. https://doi.org/10.1002/anie.202106721.
45. Li, R.-J., Tarzia, A., Posligua, V., Jelfs, K.E., Sanchez, N., Marcus, A., Baksi, A., Clever, G.H., Fadaei-Tirani, F., and Severin, K. (2022). Orientational self-sorting in cuboctahedral Pd cages. Chem. Sci. *13*, 11912–11917. https://doi.org/10.1039/d2sc03856k.
46. Tarzia, A., Wolpert, E.H., Jelfs, K.E., and Pavan, G.M. (2023). Systematic exploration of accessible topologies of cage molecules via minimalistic models. Chem. Sci. *14*, 12506–12517. https://doi.org/10.1039/d3sc03991a.
47. Sudan, S., Li, R.-J., Jansze, S.M., Platzek, A., Rudolf, R., Clever, G.H., Fadaei-Tirani, F., Scopelliti, R., and Severin, K. (2021). Identification of a Heteroleptic $Pd_6L_6L'_6$ Coordination Cage by Screening of a Virtual Combinatorial Library. J. Am. Chem. Soc. *143*, 1773–1778. https://doi.org/10.1021/jacs.0c12793.
48. Prusty, S., Yazaki, K., Yoshizawa, M., and Chand, D.K. (2017). A Truncated Molecular Star. Chemistry *23*, 12456–12461. https://doi.org/10.1002/chem.201702264.
49. Howlader, P., Das, P., Zangrando, E., and Mukherjee, P.S. (2016). Urea-Functionalized Self-Assembled Molecular Prism for Heterogeneous Catalysis in Water. J. Am. Chem. Soc. *138*, 1668–1676. https://doi.org/10.1021/jacs.5b12237.
50. Tessarolo, J., Benchimol, E., Jouaiti, A., Hosseini, M.W., and Clever, G.H. (2023). Modular enhancement of circularly polarized luminescence in $Pd_2A_2B_2$ heteroleptic cages. Chem. Commun. (Camb) *59*, 3467–3470. https://doi.org/10.1039/d3cc00262d.
51. Turcani, L., Tarzia, A., Szczypiński, F.T., and Jelfs, K.E. (2021). stk: An extendable Python framework for automated molecular and supramolecular structure assembly and discovery. J. Chem. Phys. *154*, 214102. https://doi.org/10.1063/5.0049708.
52. Eastman, P., Galvelis, R., Peláez, R.P., Abreu, C.R.A., Farr, S.E., Gallicchio, E., Gorenko, A., Henry, M.M., Hu, F., Huang, J., et al. (2024). OpenMM 8: Molecular Dynamics Simulation with Machine Learning Potentials. J. Phys. Chem. B *128*, 109–116. https://doi.org/10.1021/acs.jpcb.3c06662.
53. Shaomeng, G., Mengqi, L., Cheng, L., Weiwei, Z., Honglong, H., Ning, L., and Wei-Hong, Z. (2024). Enantiospecific Photoresponsive Metallacages Based on Sterically Hindered Diarylethenes for Chiral Recognition. CCS Chem. *7*, 1005–1015. https://doi.org/10.31635/ccschem.024.202404252.
54. Walther, A., Tusha, G., Schmidt, B., Holstein, J.J., Schäfer, L.V., and Clever, G.H. (2024). Solvent-Directed Social Chiral Self-Sorting in Pd_2L_4 Coordination Cages. J. Am. Chem. Soc. *146*, 32748–32756. https://doi.org/10.1021/jacs.4c12525.